RESEARCH ARTICLE

High-speed stereoscopic PIV study of rotating instabilities in a radial vaneless diffuser

A. Dazin · G. Cavazzini · G. Pavesi ·
P. Dupont · S. Coudert · G. Ardizzon ·
G. Caignaert · G. Bois

Abstract This paper presents an experimental analysis of the unsteady phenomena developing in a vaneless diffuser of a radial flow pump. Partial flow operating conditions were investigated using 2D/3C high repetition rate PIV, coupled with unsteady pressure transducers. Pressure measurements were acquired on the shroud wall of the vaneless diffuser and on the suction pipe of the pump, whereas PIV flow fields were determined on three different heights in the hub to shroud direction, inside the diffuser. The classical Fourier analysis was applied to both pressure signals to identify the spectral characteristics of the developing instabilities, and the high-order spectral analysis was exploited to investigate possible non-linear interaction mechanisms between different unsteady structures. A dedicated PIV averaging procedure was developed and applied to the PIV flow fields so as to capture and visualize the topology of the spectrally identified phenomena. The influence of these phenomena on the diffuser efficiency was also investigated.

1 Introduction

The development of instabilities insides turbomachines negatively affects their performance in terms of efficiency, vibrations, stability and noise emission.

Several studies have been carried out over the years to understand the characteristics and the causes of perturbing unsteady phenomena developing in different types of operating machines.

Among these phenomena, the rotating stall in centrifugal compressors is undoubtedly one of the most studied in the last decades. Theoretical analyses (Jansen 1964; Senoo and Kinoshita 1977; Abdelhamid 1983; Fringe and Van den Braembussche 1984, 1985; Tsujimoto et al. 1996; Dou and Mizuki 1998), as well as experimental and numerical analyses (Kinoshita and Senoo 1985; Nishida and Kobayshi 1988; Kobayshi and Nishida 1990; Ferrara et al. 2002a, b, 2006; Cellai et al. 2003a, b; Carnevale et al. 2006; Ljevar et al. 2006; Chuang et al. 2007; Dazin et al. 2008), were carried out to study the characteristics of the rotating stall, the geometrical and flow parameters affecting it, and the flow mechanisms that can lead to its occurrence.

Analogous interest was directed towards the stall phenomena developing inside the pumps. In more recent years, Pedersen et al. (2003) experimentally identified a steady two-channel stall phenomenon inside a pump impeller at quarter design flow rate. This spatially stable stall phenomenon developing inside the impeller was also captured by Krause et al. (2005), which demonstrated its evolution towards a rotating stall at lower flow rates. Rotating stall inside vaned diffuser was identified and studied by Sinha et al. (2001), Sano et al. (2002a, b), Guleren and Pinarbasi (2004).

Several experimental and numerical analyses were also carried out on the unsteady phenomena connected with the interaction between rotor and stator elements. Unsteady flows and pressure fluctuations developing inside centrifugal pumps and their connection with the impeller/diffuser geometries and with the operating conditions were studied by Arndt et al. (1989, 1990), Dong et al. (1997), Fatsis et al. (1997), Parrondo-Gayo et al. (2002), Wuibaut et al. (2002), Guo and Okamoto (2003), Furukawa et al. (2003), Hong and Kang (2004), Akhras et al. (2004), Guo and Maruta (2005), Majidi (2005), Rodriguez et al. (2007), Pavesi et al. (2008), Cavazzini et al. (2009) and Feng et al. (2009).

Even though the understanding of the unsteady phenomena developing in the turbomachines was improved by the above listed analyses, however, the characteristics and flow mechanisms of this unsteadiness were not completely explained.

The present paper is focused on the so-called "unforced unsteadiness" of the flow in a radial flow pump, (Fernandez Oro et al. 2009), i.e. on the unsteady phenomena not connected with the blade passage frequency.

The aim of the research was to identify, characterize and visualize the instabilities developing inside a radial vaneless diffuser. Whereas previous experimental investigations of this kind of instabilities were conducted using measurement techniques resolved either in time or in space, the aim of this research was to catch better the spatio-temporal evolution of the phenomenon with the help of a measurement technique resolved both in time and space. For that purpose, experimental results obtained at partial loads by means of high repetition rate PIV coupled with unsteady pressure transducers were obtained and are presented in this paper. These data also allowed exploring the 3D behaviour of the phenomenon as three components PIV maps were obtained at three heights within the diffuser. The linear and non-linear spectral analysis was applied to the signals in order to spectrally characterize the unsteady phenomena. Then, a dedicated phase-averaging technique, based on the spectral results, was developed to capture and visualize the unsteadiness evolution. Finally, the effects of the instability development on the diffuser efficiency were also analysed.

2 Experimental set-up

The experimental analysis was carried out on the so-called SHF impeller (Fig. 1) coupled with a vaneless diffuser. The specific speed ω_s and radius R_s of the centrifugal impeller are:

$$\omega_s = \omega \frac{q_{BEP}^{1/2}}{(\Delta P_{BEP}/\rho)^{3/4}} = 0.577$$

$$R_s = R_2 \frac{(\Delta P_{BEP}/\rho)^{3/4}}{q_{BEP}^{1/2}} = 2.43$$

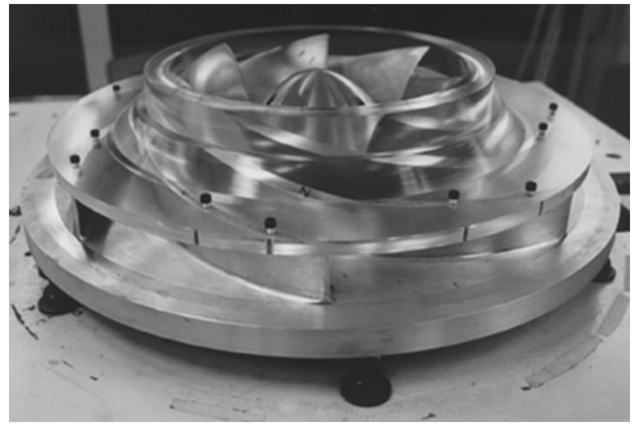

Fig. 1 SHF impeller

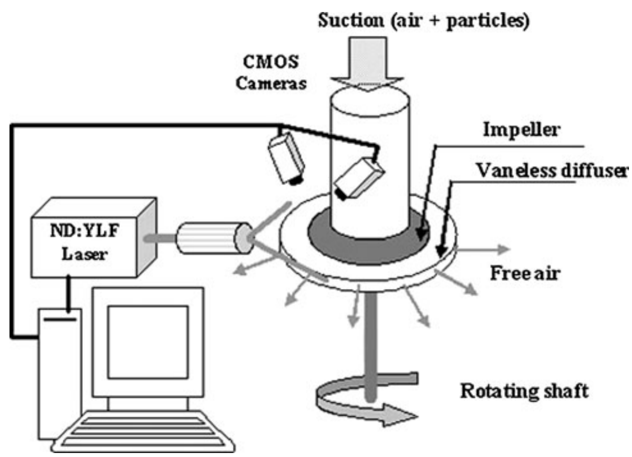

Fig. 2 Experimental set-up

where ω is the angular speed of the impeller, R_2 its outlet radius, ρ the density of the fluid, q_{BEP} and ΔP_{BEP}, respectively, the volume flow rate and the total pressure rise of the impeller at best efficiency point.

The tests were made in air with a test rig (Fig. 2) developed for studying the rotor–stator interaction phenomena. Since the analysis was focused on the impeller-diffuser interaction, no volute was used downstream the diffuser in order to guarantee the axial-symmetry of the pressure field at the pump discharge.

The test rig is properly built for the application of optical analysis methods and in particular of the particle image velocimetry (PIV) technique: the walls of the diffuser are transparent, and the lack of volute downstream the diffuser allows large optical access for the laser sheet and the cameras. It was already used in previous studies carried out on the same impeller coupled with a short vaneless diffuser (Wuibaut et al. 2001a and b, 2002) and a vaned diffuser (Cavazzini et al. 2009).

Table 1 Pump characteristics

SHF impeller characteristics		
R_1	Impeller tip inlet radius	141.1 mm
R_2	Impeller outlet radius	256.6 mm
b_2	Impeller outlet width	38.5 mm
β_{2c}	Outlet blade angle (measured from the peripheral velocity)	22.5°
S	Mean blade thickness	9 mm
Z	Number of impeller blades	7
Q_{des}	Design flow rate at 1,200 rpm	0.236 m^3/s
N	Impeller rotation velocity	1,200 rpm
$Re = R_2^2\omega/\nu$	Reynolds number	5.52×10^5
Vaneless diffuser characteristics		
R_3	Diffuser inlet radius	257.1 mm
R_4	Diffuser outlet radius	390 mm
b_3	Diffuser constant width	40 mm

In the present study, to favour the complete development and stabilization of the unsteady interaction phenomena at the impeller discharge, a vaneless diffuser having an outlet radius larger than the previous one was coupled with the impeller. The main geometrical characteristics of the analysed configuration together with the design operating point are reported in Table 1.

The flow field inside the diffuser was studied at several flow rates by means of 2D/3C high-speed PIV and pressure transducers.

The laser illumination system consists of two independent Nd:YLF laser cavities, each of them producing about 20 mJ per pulse at a pulse frequency of 980 Hz. The pulse duration is 90 ns. A light sheet approximately 90 mm wide with a thickness of 1.5 mm was obtained at three heights in the hub to shroud direction ($b/b_3 = 0.25$, 0.5 and 0.75—see Fig. 3) using conventional optical components (two spherical and a cylindrical lenses). The time delay between the first and the second cavity pulses was settled to 110/130 μs, depending on the flow rate.

Two CMOS cameras (1,680 × 930 pixel^2), equipped with 50 mm lenses, were properly synchronized with the laser pulses. They were located at a distance of 480 mm from the measurement regions. The angle between the object plane and the image plane was about 45°.

As regards the seeding, incense smoke particles having a size of less than 1 μm (Cheng et al. 1995) were used. These particles were introduced near the inlet of the pump, but, as the experiments were conducted in a closed room, the whole room was seeded after few minutes of operation. The mean image particle size, estimated by image treatment, was 1.7 pixels and about 17 particles were identified in each correlation window of 32 × 32 pixel^2.

The image treatment was performed by a software developed by the Laboratoire de Mecanique de Lille. The

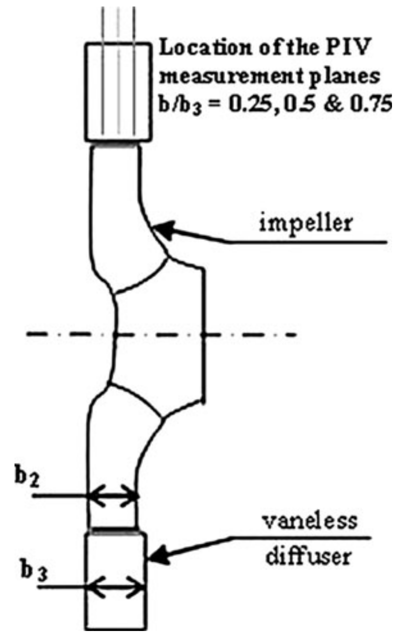

Fig. 3 Cross-section of the pump and location of the measurement laser planes

cross-correlation technique was applied to the image pairs with a correlation window size of 32 × 32 pixels^2 and an overlapping of 50%, obtaining flow fields of 80 × 120 mm^2 and 81 × 125 velocity vectors. The correlation peaks were fitted with a three-point Gaussian model. Concerning the stereoscopic reconstruction, the method first proposed by Soloff et al. (1997) was used. A velocity map spanned nearly all the diffuser extension in the radial direction, whereas in the tangential one was covering an angular portion of about 14°.

A rms uncertainty value of 1.3 pixel was obtained through the PIV analysis of a quiescent flow. Other error sources were estimated on the basis of an uncertainty analysis conducted on synthetic PIV images (Foucaut et al. 2004). In particular, the following uncertainties were determined: 0.05 pixel for peak-locking, 0.01 pixel due to the particle loss linked with the velocity component normal to the laser sheet and less than 0.15 pixels due to velocity gradients. The accuracy of the reconstruction algorithm was estimated to be of about 0.1 pixel (Perenne et al. 2003). As the particle displacements were of the order of 10 pixels, the total PIV uncertainty was estimated to be less than 5%.

Each PIV measurement campaign was carried out for a time period of 1.6 s, corresponding to 32 impeller revolutions at a rotation speed of 1,200 rpm. Since the temporal resolution of the acquisition was of 980 velocity maps per second, the time period of 1.6 s allowed obtaining 1,568 consecutives velocity maps, corresponding to about 49 velocity maps per impeller revolution For each analysed operating condition and each laser sheet height, the measurement campaign was repeated twice, obtaining two data sets of 1,568 velocity maps.

Four Brüel and Kjaer condenser microphones (Type 4135) simultaneously measured the unsteady pressure. The measurement uncertainty for these measurements was less than 1%. The measured data were acquired by a LMS Difa-Scadas system with a sampling frequency of 2,048 Hz. Two of these microphones were placed flush with the diffuser shroud wall at the same radial position ($r/R_3 = 1.05$) but at different angular position ($\Delta\theta = 75°$), whereas the other two were located on the suction pipe of the pump, 150 mm upstream the impeller inlet. To synchronize the unsteady pressure measurements with the velocity maps, a signal was sent by the PIV system to the LMS Difa-Scadas acquisition system.

Experimental measurements were acquired for the design flow rate Q_{des} and at five partial flow rates (0.26 Q_{des}, 0.45 Q_{des}, 0.56 Q_{des}, 0.66 Q_{des} and 0.75 Q_{des}) with an impeller rotation speed of 1,200 rpm.

The results presented in this paper refer mainly to the lowest analysed flow rate, which is 0.26 Q_{des}.

3 Results

3.1 Fourier analysis

The results of a Fourier analysis carried out on the pressure fluctuations measured in the vaneless diffuser were already presented in a previous paper (Dazin et al. 2008) and are briefly summarized here.

Figure 4 reports the comparison of the cross-power spectra of the unsteady pressure signals acquired by the microphones located in the diffuser at the design flow rate Q_{des} and at a partial load (0.26 Q_{des}). Amplitudes were scaled by $\left(1/2\rho R_2^2\omega_{imp}^2\right)^2$ and frequencies by the impeller rotation frequency f_{imp}.

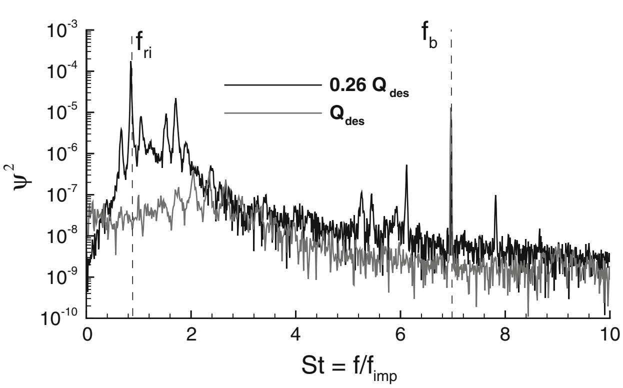

Fig. 4 Comparison of the cross-power spectra of the unsteady pressure signals acquired by two microphones located at the diffuser inlet at the design flow rate Q_{des} and at 0.26 Q_{des}

The cross-spectrum at the design flow rate is clearly dominated by the blade passage frequency f_b ($7{\cdot}f_{imp}$). The $Q = 0.26\ Q_{des}$ spectrum is overcome by several peaks in the frequency band between 0.5 f_{imp} and 2.0 f_{imp}, particularly by the frequency $f/f_{imp} = 0.84$, that was demonstrated, by the analysis of the amplitude and phase of the cross-power spectra of the two transducers located in the vaneless diffuser (Dazin et al. 2008), to be the fundamental frequency of a rotating instability composed by three cells rotating around the impeller discharge with an angular velocity equal to 28% of the impeller rotation velocity.

The instability characteristics (number of cells and velocity) were compared with the results of linear stability analysis of the core flow of a vaneless diffuser proposed by Tsujimoto et al. (1996) for 2D non-viscous flow: this theoretical analysis predicts the critical flow angle α_3 at the inlet of the diffuser under which the flow is unstable for a given number of cells m and a given outlet to inlet diffuser radius ratio R_4/R_3.

For the geometrical configuration considered in this study ($R_4/R_3 = 1.5$), the predicted critical angle was

- 3° for a one-cell instability,
- 6° for a 2-cell instability,
- 10° for a 3-cell instability.

The experimental flow angle at diffuser inlet, determined on the basis of the velocity triangles at the outlet of a centrifugal impeller, was estimated to be 6°. For this angle, according to the theoretical analysis, the only unstable configuration is the 3-cell mode, whereas the 1-cell mode is stable as well as the 2-cell mode, characterized by a neutral stability.

The good agreement of the experimental results with the linear stability analysis in terms of number of cells was further confirmed by the comparison in terms of instability velocity that was predicted to be 28% of the impeller velocity.

The other low-frequency peaks identified in Fig. 4 around the fundamental frequency were thought to be spectral components generated by the non-linear interaction between the frequency of the instability and the impeller frequency f_{imp}. To verify this hypothesis of non-linear coupling, and furthermore, to exclude the presence of other fundamental frequencies, a high-order non-linear spectral analysis was carried out on the unsteady pressure signals. This analysis allowed to measure the non-linear dependence between three spectral components (k, l, $k + l$), i.e. to distinguish between spontaneously excited modes and coupled modes, and hence to identify the self-excited peaks that dominate the spectra. In particular, the normalized third-order spectrum of a signal $x(t)$, known as "bi-coherence", (Akin and Rockwell 1994; Knisely and Rockwell 1982; Rosenblatt and Van Ness 1965; Nikias and Mendel 1993; Nikias and Petropulu 1993) was used and determined as:

$$b^2(k,l) = \frac{|B(k,l)|^2}{P(k)P(l)P(k+l)}$$

where P is the power spectrum, k and l are frequency indices, and B is the third-order spectrum of a signal $x(t)$, i.e. the "bi-spectrum", defined as:

$$B(k,l) = E[X(k)X(l)X^*(k+l)]$$

(X is the Fourier Transform of the signal $x(t)$, X^* denotes its complex conjugate).

The bi-coherence of the pressure signals was estimated by means of a direct FFT-based method. The signals were segmented into 2,048 non-overlapping segments and windowed by a Hanning function in the time domain. To determine the bi-coherence, the bi-spectrum $B(k,l)$ and the power spectrum $P(k)$ were averaged, respectively, across the bi-spectra $B_i(k,l)$ and the power spectra $P_i(k)$ of the signal segments, determined as:

$$B_i(k,l) = X_i(k)X_i(l)X_i^*(k+l)$$

$$P_i(k) = |X_i(k)|^2$$

where X_i denotes the FFT of i-th segment and X_i* its complex conjugate. The bi-coherence has a non-zero value falling between 0 and 1, when the components are non-linearly coupled.

Figure 5 reports the bi-coherence of the pressure signals acquired by the microphones located in the diffuser for $Q/Q_{\mathrm{des}} = 0.26$. The bi-coherence presents several peaks, testifying a non-linear coupling between the phenomena. In particular, all the low frequencies peaks located around the fundamental frequency of the instability, resulted from the non-linear interaction between the rotating instability $f/f_{\mathrm{imp}} = 0.84$ and the impeller passage frequency $f/f_{\mathrm{imp}} = 7.00$.

3.2 PIV averaged results

3.2.1 Averaging procedure

To experimentally capture and visualize the unsteady flow field associated with the spectrally identified instability, an appropriate method of averaging the velocity fields was developed. According to this method, the PIV velocity maps were properly combined on the basis of the determined instability precession velocity (0.28 ω_{imp}) and an averaged flow field in a reference frame rotating with the instability was obtained.

The following steps characterize the averaging method.

First, since the measurements were not synchronized with the instability rotation, the velocity maps could not be

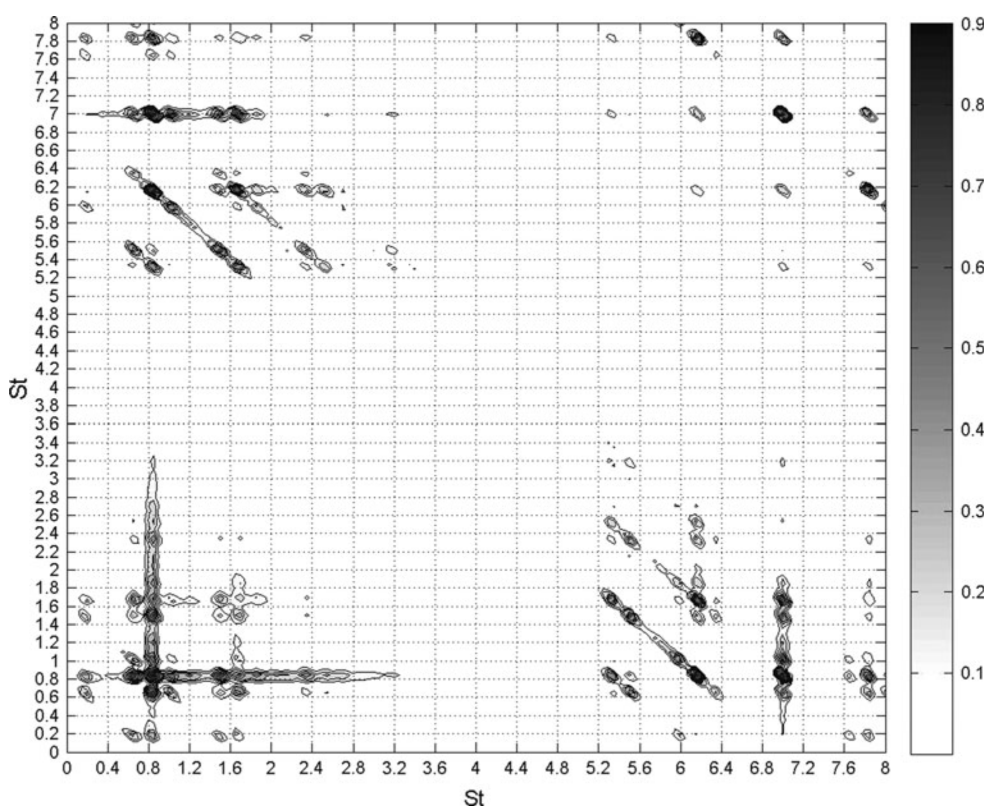

Fig. 5 Bi-coherence of the pressure signals acquired by the microphones located in the diffuser for $Q/Q_{\mathrm{des}} = 0.26$

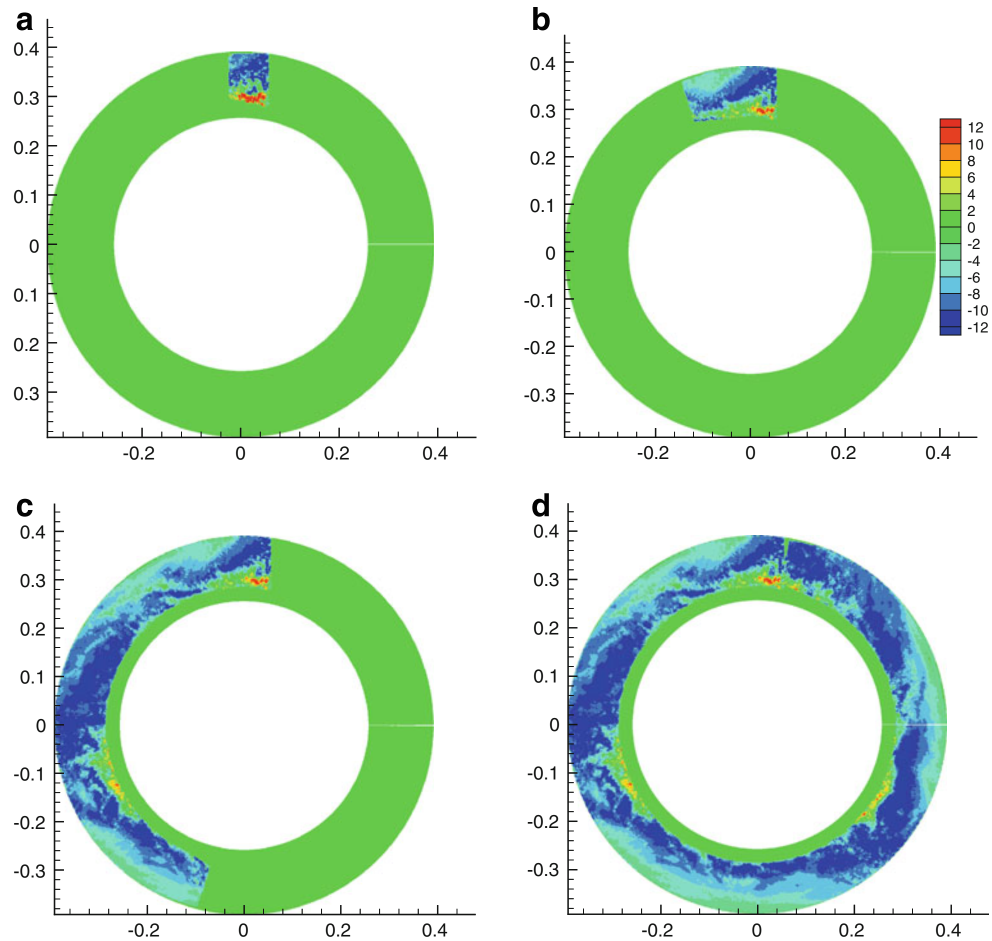

Fig. 6 Averaging computation results after 1, 10, 80 and 175 velocity maps for the tangential velocity component at mid-span

exactly superimposed at each impeller revolution. For this reason, a reference grid having dimensions equal to that of the diffuser ($0 < \theta < 360°$, $0.257 < r < 0.390$ m) was created. To have an almost direct correspondence between this mesh and the PIV grid, the size of one cell of the mesh was fixed roughly equal to the size of one cell of the PIV grid.

Then, the first velocity map was bi-linearly interpolated on the new grid, as shown for the tangential velocities in Fig. 6a. The velocity values of the mesh were fixed equal to zero except in the zone corresponding to the first PIV map properly interpolated on the grid.

Since the reference frame was fixed to rotate with the instability, the second velocity map was added in the new mesh after a rotation of an angle equal to the instability velocity multiplied by the sampling period of the PIV measurements. As this second velocity map overlapped the first one, in the overlapping zone the velocity values were properly averaged. This operation was repeated for the following velocity maps till a complete revolution of the instability, corresponding to 175 maps, was made. Afterwards, the maps were averaged with the ones of the previous revolution(s). Examples of the averaging computation results respectively after 10, 80 and 175 velocity maps are reported in Fig. 6b–d.

At the end of the procedure, 120 velocity vectors were averaged in each point of the grid to obtain a mean velocity vector. The standard deviation was of the order of 2 m/s and the corresponding 95% confidence interval for each averaged velocity component $\bar{c}_i$ was:

$[\bar{c}_i \pm 0.4 \text{ m/s}]$

3.2.2 *Averaged results*

The procedure described above allowed to obtain averaged flow fields in a reference frame rotating with the instability for the three velocity components ($\bar{c}_r, \bar{c}_u$ and $\bar{c}_z$). Results obtained at mid-height are reported in Fig. 7. Because of the laser sheet reflections on the impeller blades, several instantaneous flow fields were negatively affected at the diffuser inlet by the proximity of the impeller blades. For this reason, the averaged flow fields are presented only for $r > 0.3$ m.

Fig. 7 Results of the averaging of 1,581 consecutive velocity maps in a reference frame rotating with the instability at $Q/Q_{des} = 0.26$: radial (**a**), tangential (**b**) and axial averaged flow fields (**c**) and velocity vectors (**d**) at mid-height of the diffuser (Velocities in m/s)

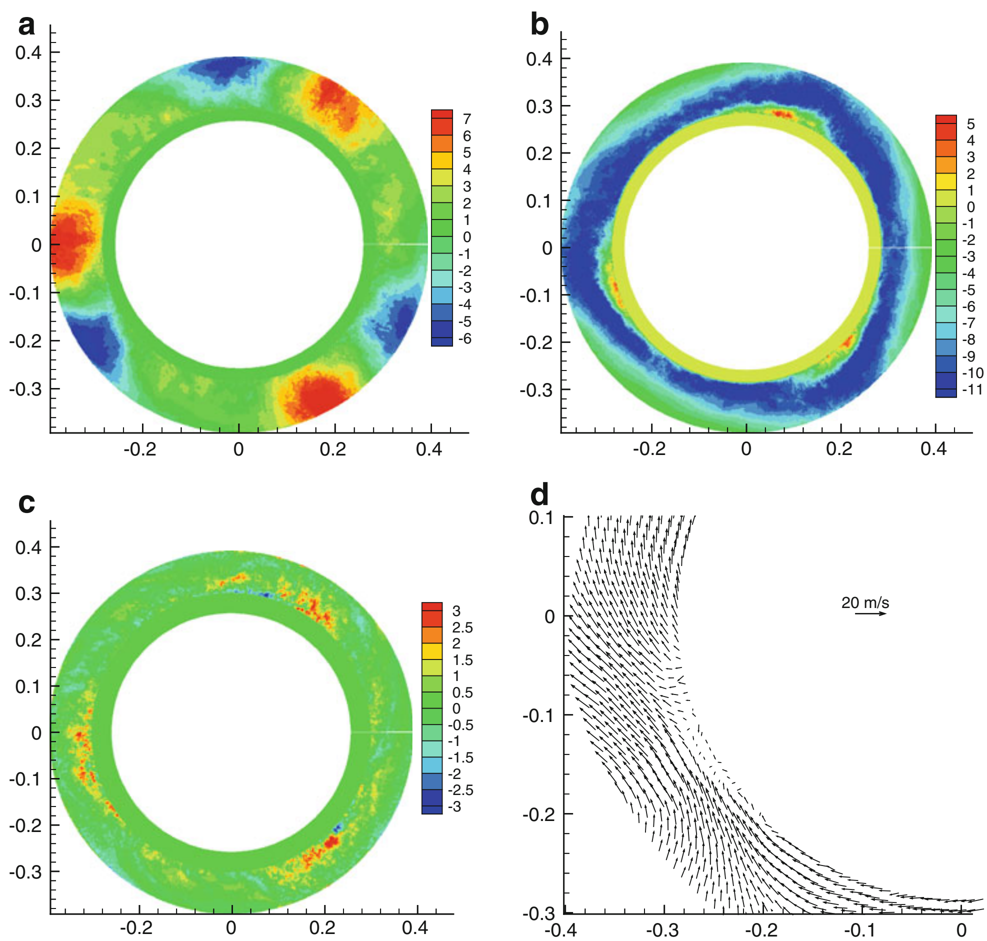

Three patterns having similar topologies are clearly identifiable in the radial velocity component plots (Fig. 7a). They are composed of two cores, respectively, of inward and outward radial velocities, located near the diffuser outlet (Fig. 7b and d). In correspondence to these two cores, a zone of negative tangential velocity is identifiable in all three planes near the diffuser inlet and a zone of slightly positive axial velocity is outlined at mid-span (Fig. 7c). The patterns' intensity and therefore their definition are greater at mid-span than on the other two heights (Figs. 8 and 9).

To investigate more in-depth the diffuser behaviour and to better understand the possible origin of this rotating instability, two more parameters were determined from the results of the averaging procedure: the circumferential averages at a given radius of the radial velocity component

Fig. 8 Results of the averaging of 1,581 consecutive velocity maps in a reference frame rotating with the instability at $Q/Q_{des} = 0.26$: radial (**a**) and tangential (**b**) velocity components at hub side ($b/b_3 = 0.25$). (Velocities in m/s.)

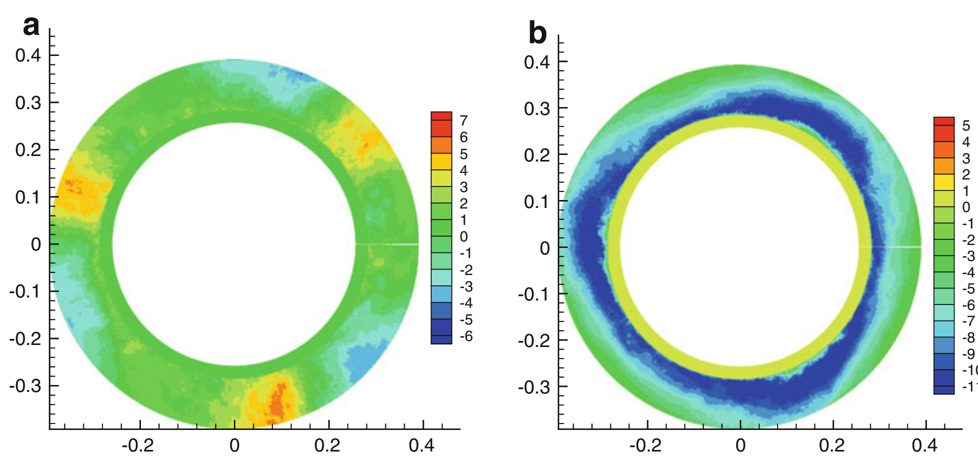

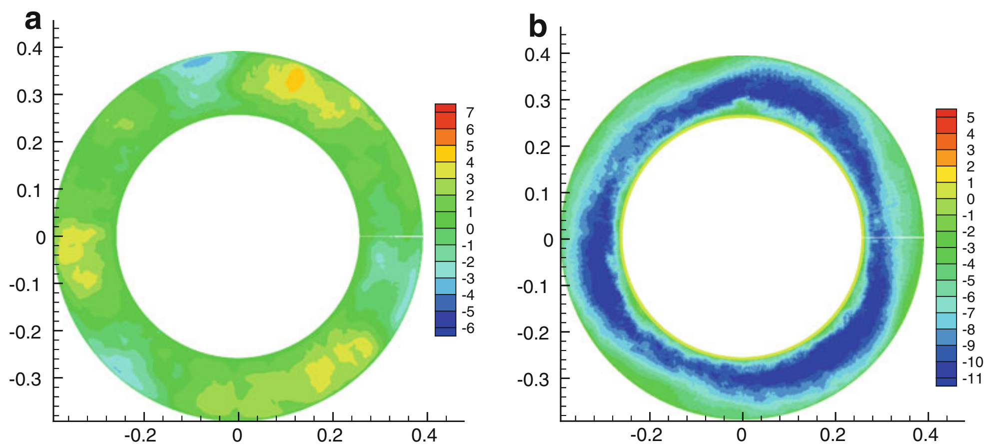

Fig. 9 Results of the averaging of 1,581 consecutive velocity maps in a reference frame rotating with the instability at $Q/Q_{des} = 0.26$: radial (**a**) and tangential (**b**) velocity components at shroud side ($b/b_3 = 0.75$). (Velocities in m/s.)

$\overline{\overline{c_r}}$ and of the product of the averaged radial and tangential velocity components $\overline{\overline{c_r} \cdot \overline{c_u}}$:

$$\overline{\overline{c_r}} = \frac{1}{2\pi} \int_0^{2\pi} \overline{c_r} \mathrm{d}\theta$$

$$\overline{\overline{c_u} \cdot \overline{c_r}} = \frac{1}{2\pi} \int_0^{2\pi} \overline{c_u} \cdot \overline{c_r} \mathrm{d}\theta$$

Figure 10a shows the evolution of the quantity $r\bar{\bar{c}}_r$ as a function of the radius on the three analysed heights, in comparison with theoretical value of $r\bar{\bar{c}}_r|_{th}$ calculated in the hypothesis of a one-dimensional flow field:

$$r \cdot \overline{\overline{c_r}}\Big|_{th} = \frac{Q}{2\pi b_3}$$

For $r = 0.3$ m, the value of $r \cdot \bar{\bar{c}}_r$ is greater than the theoretical value in all the three planes. This could be due to a boundary layer detachment on the diffuser walls that determined a concentration of the flow rate far from the walls, between $b/b_3 = 0.25$ and $b/b_3 = 0.75$.

For greater radii (0.3 m $< r <$ 0.35 m), the quantity $r \cdot \bar{\bar{c}}_r$ progressively decreases on the hub side ($b/b_3 = 0.25$) and increases on the shroud side ($b/b_3 = 0.75$). This behaviour could be justified by a blockage of the flow near the hub with a consequent migration of the flow rate towards the shroud. The presence of the blockage on the hub, together with the development of a secondary flow in the hub to shroud direction, was confirmed by the analysis of the positive values of the axial velocity $\overline{C_a}$ in the average flow field at mid-span (Fig. 7) and in the instantaneous flow fields not perturbed by laser reflections. These flow fields were characterized by two zones of opposite values of axial velocity (Fig. 11a—mid-span) that suggested the existence of a vortex developing in the hub-to-shroud direction and partially blocking the flow coming out from the impeller discharge. The position of this vortex

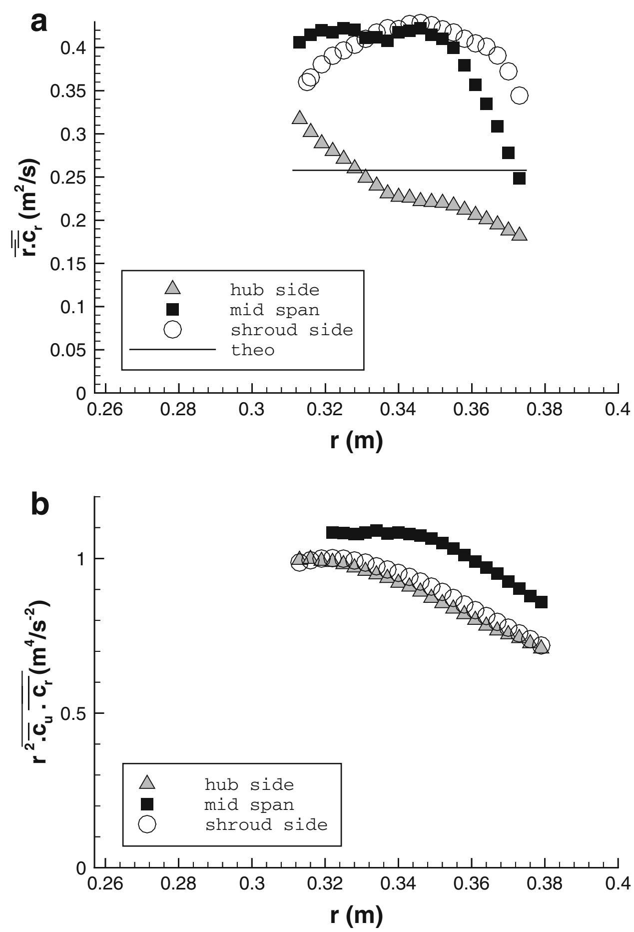

Fig. 10 Evolutions of $r \cdot \bar{\bar{c}}_r$ (**a**) and $r^2 \cdot \overline{\bar{c}_r \times \bar{c}_u}$ (**b**) as a function of the radius for $Q/Q_{des} = 0.26$

oscillated with a time-depending intensity from hub to mid-span (Fig. 12) and in the radial direction (Fig. 13).

Finally, in the last part of the diffuser ($r > 0.35$ m), all three measurement heights are characterized by a progressive decrease of $r \cdot \bar{\bar{c}}_r$ with a reduction in the differences between their corresponding values and an approach

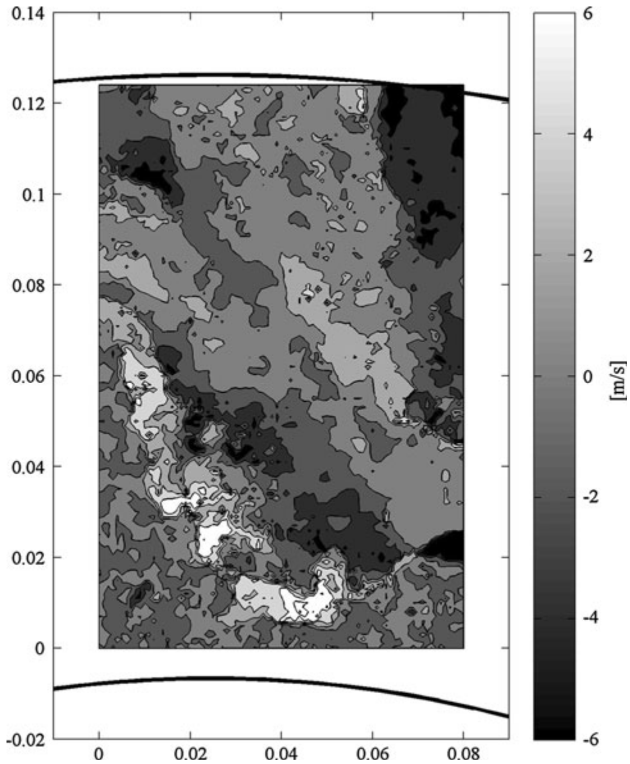

Fig. 11 Map of the instantaneous axial velocity component at mid-span (instant t_1)

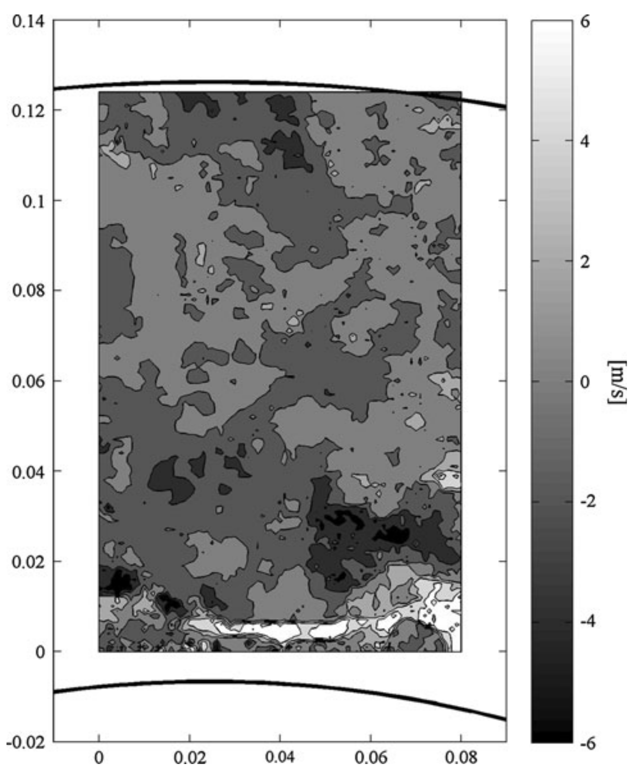

Fig. 12 Map of the instantaneous axial velocity component on the hub side

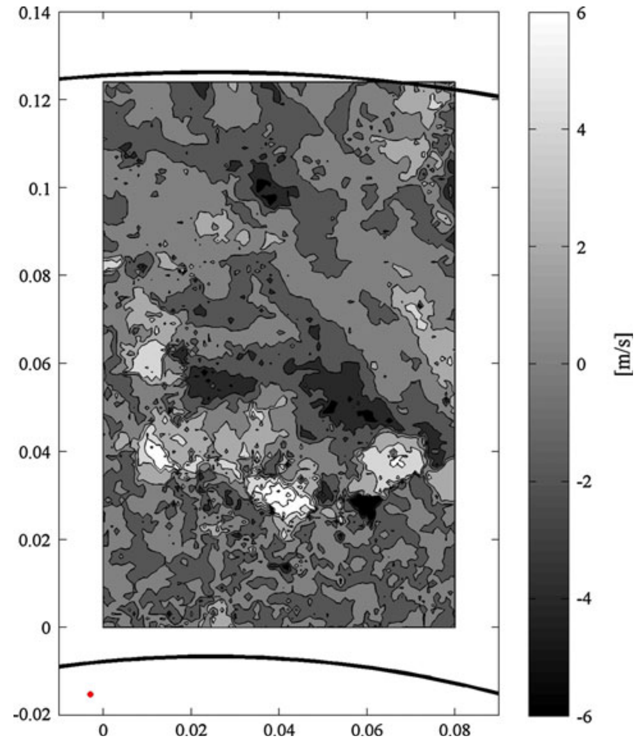

Fig. 13 Map of the instantaneous axial velocity component at mid-span (instant t_2). The red point is the position of the impeller trailing edge

towards the theoretical one. This behaviour suggested a homogenization of the flow rate along the diffuser width.

To verify the effects of the development of the instability on the diffuser efficiency, the evolution of the quantity $r^2 \cdot \overline{\bar{c}_r \bar{c}_u}$ as a function of the radius on the three heights was considered (Fig. 10b). This quantity represents the moment of momentum per unit of diffuser height and angle, divided by the density. In an ideal case with no losses, this moment would keep constant inside the entire diffuser.

As it can be seen, in all the investigated heights, this parameter is characterized by a decrease of about 30% in the last two thirds of the diffuser (0.30 m $< r < 0.39$ m). Since the rotating instability was demonstrated to increase its intensity in this zone, the highlighted momentum decay seemed to be associated with it and in particular with the cores of inward and outward radial velocity previously identified (Figs. 7, 8 and 9).

4 Conclusions

An experimental analysis was carried out on a vaneless diffuser of a radial flow pump to investigate the development of unsteady phenomena at partial flow rates.

Measurements were performed at the design flow rate and at partial loads with a high repetition rate PIV coupled with unsteady pressure transducers placed flush with the diffuser shroud wall. Three different planes in the hub-to-shroud direction were experimentally investigated.

The spectral analysis, applied to the pressure signals, confirmed the presence of a rotating instability developing inside the vaneless diffuser. The development of mechanisms of non-linear interaction between the instability and the impeller frequency was also highlighted by the high-order spectral analysis with a consequent increasing number of low-frequency peaks in the spectra.

A dedicated phase-averaging technique properly applied on the PIV flow fields on the basis of the spectral analysis results allowed visualizing of a three-cell rotating structure. Each cell of this structure resulted to be composed by two cores of inward and outward radial velocity and by a zone of negative tangential velocity.

The analysis of the radial evolution of the averaged velocity components highlighted the possible presence of a blockage near the entrance of the diffuser on the hub side. This blockage, due to a vortex developing in the hub-to-shroud direction, seemed to be the cause of a migration of the flow rate towards the shroud side. In the second part of the diffuser, the flow field, characterized by the presence of the cores of inward and outward radial velocity showed a homogenization of the flow rate along the diffuser width. The development of these cores determined a decay of the diffuser performance, as demonstrated by the analysis of the evolution of the moment of momentum in the radial direction.

Acknowledgments The authors wish to thank the Nord Pas de Calais region and the International Campus on Safety and Intermodality in Transportation (CISIT) for their support to this research project.

References

Abdelhamid AN (1983) Effects of vaneless diffuser geometry on flow instability in centrifugal compressor systems. Can Aeronaut Space J 26(2):259–266

Akhras A, El Hajem M, Champagne J-Y, Morel R (2004) The flow rate influence on the interaction of a radial pump impeller and the diffuser. Int J Rotat Mach 10(4):309–317

Akin O, Rockwell D (1994) Actively controlled radial flow pumping system: manipulation of spectral content of wakes and wake-blade interactions. ASME J Fluids Eng 116:528–537

Arndt N, Acosta AJ, Brennen CE, Caughey TK (1989) Rotor-stator interaction in a diffuser pump. J Turbomach 111(3):213–221

Arndt N, Acosta AJ, Brennen CE, Caughey TK (1990) Experimental investigation of rotor-stator interaction in a centrifugal pump with several vaned diffusers. Trans ASME J Turbomach 112(1):98–108

Carnevale EA, Ferrara G, Ferrari L, Baldassarre L (2006) Experimental investigation and characterization of the rotating stall in a high pressure centrifugal compressor. Part VI: reduction of three impeller results. In: Proceedings of ASME, International Gas Turbine Institute, Turbo Expo 2006—power for land, sea and air, vol 6B, pp 1105–1112, Barcelona, Spain, 6–11 May 2006

Cavazzini G, Pavesi G, Ardizzon G, Dupont P, Coudert S, Caignaert G, Bois G (2009) Analysis of the rotor-stator interaction in a radial flow pump. La Houille Blanche, Revue Internationale de l'eau, n. 5/2009, pp 141–151

Cellai A, Ferrara G, Ferrari L, Megnoni CP, Baldassarre L (2003a) Experimental Investigation and characterization of the rotating stall in a high pressure centrifugal compressor. Part III: influence of diffuser geometry on stall inception and performance (2nd impeller tested). In: Proceedings of ASME, International Gas Turbine Institute, Turbo Expo, IGTI, vol 6B, pp 711–719, Atlanta, GA, United States, 16–19 June 2003

Cellai A, Ferrara G, Ferrari L, Megnoni CP, Baldassarre L (2003b) Experimental Investigation and characterization of the rotating stall in a high pressure centrifugal compressor. Part III: impeller influence on diffuser stability. In: Proceedings of ASME, International Gas Turbine Institute, Turbo Expo, IGTI, vol 6B, pp 721–728, Atlanta, GA, United States, 16–19 June 2003

Cheng YS, Bechtold WE, YU CC, Huang IF (1995) Incense smoke: characterization and dynamics in indoor environments. Aerosol Sci Technol 23:271–281

Chuang G, Chuangang G, Tong W, Bo Y (2007) Analysis of geometries' effects on rotating stall in vaneless diffuser with wavelet neural networks. Int J Rotat Mach, vol 2007, Article ID 76476, p 10. doi:10.1155/2007/76476

Dazin A, Coudert S, Dupont P, Caignaert G, Bois G (2008) Rotating instability in the vaneless diffuser of a radial flow pump. J Thermal Sci 17(4):368–374

Dong R, Chu S, Katz J (1997) Effect of modification to tongue and impeller geometry on unsteady flow, pressure fluctuations, and noise in a centrifugal pump. Trans ASME J Turbomach 119(3):506–515

Dou H-S, Mizuki S (1998) Analysis of the flow in vaneless diffusers with large width-to-radius ratios. J Turbomach 120(1):193–201

Fatsis A, Pierret S, Van den Braembussche R (1997) Three-dimensional unsteady flow and forces in centrifugal impellers with circumferential distortion of the outlet static pressure. Trans ASME J Turbomach 119(1):94–102

Feng J, Benra F-K, Dohmen HJ (2009) Unsteady flow visualization at part load conditions of a radial diffuser pump: by PIV and CFD. J Visualizat 12(1):65–72

Fernandez Oro JM, Blanco Marigorta E, Argüelles Diaz KM (2009) Forced and unforced unsteadiness in an axial turbomachine. Exp Thermal Fluid Sci 33(3):449–459

Ferrara G, Ferrari L, Megnoni CP, De Lucia M, Baldassarre L (2002a) Experimental investigation and characterization of the rotating stall in a high pressure centrifugal compressor. Part I: influence of diffuser geometry on stall inception. In: Proceedings of ASME, International Gas Turbine Institute, Turbo Expo, IGTI, vol 5A, pp 613–620, Amsterdam, The Netherlands, 3–6 June 2002

Ferrara G, Ferrari L, Megnoni CP, De Lucia M, Baldassarre L (2002b) Experimental investigation and characterization of the rotating stall in a high pressure centrifugal compressor. Part I: influence of diffuser geometry on stall performance. In: Proceedings of ASME, International Gas Turbine Institute, Turbo Expo, IGTI, vol 5A, pp 621–628, Amsterdam, The Netherlands, 3–6 June 2002

Ferrara G, Ferrari L, Baldassarre L (2006) Experimental Investigation and characterization of the rotating stall in a high pressure centrifugal compressor. Part V: Influence of diffuser geometry on stall inception and performance (3rd impeller tested). In: Proceedings of ASME, International Gas Turbine Institute, Turbo Expo 2006—Power for Land, Sea and Air, vol 6B, pp 1093–1103, Barcelona, Spain, 6–11 May 2006

Foucaut JM, Miliat B, Perenne N, Stanislas M (2004) Characterisation of different PIV algorithms using the EUROPIV synthetic image generator and real images from a turbulent boundary layer. In: Proceeding of the EUROPIV 2 workshop on particle image velocimetry. Springer, Berlin, pp 163–186

Fringe P, Van den Braembussche R (1984) Distinction between different types of impeller and diffuser rotating stall in a centrifugal compressor with vaneless diffuser. ASME J Eng Gas Turbine Power 106(2):468–474

Fringe P, Van den Braembussche R (1985) A theoretical model for rotating stall in the vaneless diffuser of a centrifugal compressor. ASME J Eng Gas Turbine Power 107(2):507–513

Furukawa A, Takahara H, Nakagawa T, Ono Y (2003) Pressure fluctuation in a vaned diffuser downstream from a centrifugal pump impeller. Int J Rotat Mach 9(4):285–292

Guleren KM, Pinarbasi A (2004) Numerical simulation of the stalled flow within a vaned centrifugal pump. Proc Inst Mech Eng C J Mech Eng Sci 218:425–435

Guo S, Maruta Y (2005) Experimental investigations on pressure fluctuations and vibration of the impeller in a centrifugal pump with vaned diffusers. JSME Int J Ser B 48(1):136–143

Guo S, Okamoto H (2003) An experimental study on the fluid forces induced by rotor-stator interaction in a centrifugal pump. Int J Rotat Mach 9(2):135–144

Hong S-S, Kang S-H (2004) Flow at the centrifugal pump impeller exit with the circumferential distortion of the outlet static pressure. Trans ASME J Fluid Eng 126(1):81–86

Jansen W (1964) Rotating stall in a radial vaneless diffuser. J Basic Eng 86:750–758

Kinoshita Y, Senoo Y (1985) Rotating stall induced in vaneless diffusers of very low specific speed centrifugal blowers. J Eng Gas Turbine Power 107(2):514–521

Knisely C, Rockwell D (1982) Self-sustained low-frequency components in an impinging shear layer. J Fluid Mech 116:157–186

Kobayshi H, Nishida H (1990) A study on the rotating stall of centrifugal compressor (2nd report, effect of vaneless diffuser inlet shape on rotating stall). Trans JSME Ser B 56(529):98–103

Krause N, Zähringer K, Pap E (2005) Time-resolved particle image Velocimetry for the investigation of rotating stall in a radial pump. Exp Fluids 39:192–201. doi:10.1007/s00348-005-0935-2

Ljevar S, de Lange HC, van Steenhoven AA (2006) Two-dimensional rotating stall analysis in a wide vaneless diffuser. Int J Rotat Mach, vol 2006, Article ID 56420, pp 1–11. doi:10.115/IJRM/2006/56420

Majidi K (2005) Numerical study of unsteady flow in a centrifugal pump. Trans ASME J Turbomach 127(2):363–371

Nikias CL, Mendel JM (1993) Signal processing with high-order spectra. IEEE Signal Process Mag 10(3):10–37

Nikias CL, Petropulu AP (1993) High-order spectral analysis: a non-linear signal processing framework. Prentice Hall, New Jersey

Nishida H, Kobayshi H (1988) A study on the rotating stall of centrifugal compressor (1st report, effect of vaneless diffuser width on rotating stall). Trans JSME Ser B 54(499):584–594

Parrondo-gayo JL, Gonzalez-perez J, Fernandez-francos J (2002) The effect of the operating point on the pressure fluctuations at the blade passage frequency in the volute of a centrifugal pump. Trans ASME J Fluid Eng 124(3):784–790

Pavesi G, Cavazzini G, Ardizzon G (2008) Time-frequency characterization of the unsteady phenomena in a centrifugal pump. Int J Heat Fluid Flow 29(5):1527–1540

Pedersen N, Larsen PS, Jacobsen CB (2003) Flow in a centrifugal pump impeller at design and off-design conditions. Part I: particle image velocimetry (PIV) and laser doppler velocimetry (LDV) measurements. ASME J Fluids Eng 125:61–72

Perenne N, Foucaut JM, Savatier J (2003) Study of the accuracy of different stereoscopic reconstruction algorithms. In: Proceeding of the EUROPIV 2 workshop on particle image velocimetry. Springer-Verlag, berlin, pp 375–390

Rodriguez CG, Egusquiza E, Santos IF (2007) Frequencies in the vibration induced by the rotor stator interaction in a centrifugal pump turbine. Trans ASME J Fluid Eng 129(11):1428–1435

Rosenblatt M, van Ness JW (1965) Estimation of the Bispectrum. Ann Math Stat 36:1120–1136

Sano T, Nakamura Y, Yoshida Y, Tsujimoto Y (2002a) Alternate blade stall and rotating stall in a vaned diffuser. JSME Int J Ser B 45(4):810–819

Sano T, Yoshida Y, Tsujimoto Y, Nakamura Y, Matsushima T (2002b) Numerical study of rotating stall in a pump vaned diffuser. ASME J Fluids Eng 124:363–370

Senoo Y, Kinoshita Y (1977) Influence of inlet flow conditions and geometries of centrifugal vaneless diffusers on critical flow angle for reverse flow. J Fluid Mech 99(1):98–103

Sinha M, Pinarbasi A, Katz J (2001) The flow structure during onset and developed states of rotating stall within a vaned diffuser of a centrifugal pump. ASME J Fluids Eng 123:490–499

Soloff SM, Adrian RJ, Liu ZC (1997) Distortion compensation for generalized stereoscopic particle image velocimetry. Meas Sci Technol 8:1441–1454

Tsujimoto Y, Yoshida Y, Mori Y (1996) Study of vaneless diffuser rotating stall based on two dimensional inviscid flow analysis. ASME J Fluids Eng 118:123–127

Wuibaut G, Dupont P, Bois G, Caignaert G, Stanislas M (2001a) Analysis of flow velocities within the impeller and the vaneless diffuser of a radial flow pump. ImechE J Power Energy A 215:801–808

Wuibaut G, Dupont P, Bois G, Caignaert G, Stanislas M (2001b) Application de la vélocimétrie par images de particules à la mesure simultanée de champs d'écoulements dans la roue et le diffuseur d'une pompe centrifuge. La Houille Blanche, revue internationale de l'eau, N° 2/2001, pp 75–80

Wuibaut G, Bois G, Dupont P, Caignaert G, Stanislas M (2002) PIV measurements in the impeller and the vaneless diffuser of a radial flow pump in design and off-design operating conditions. J Fluid Eng 124(3):791–797